

SUT-NANOTEC-SLRI beamline for X-ray absorption spectroscopy

Wantana Klysubun,^{a*} Pinit Kidkhunthod,^a Pongjakk Tarawarakarn,^a Panidtha Sombunchoo,^a Chanapa Kongmark,^b Sukit Limpijumnong,^c Saroj Rujirawat,^c Rattikorn Yimnirun,^c Gamolwan Tumcharern^d and Kajornsak Faungnawakij^d

Received 2 December 2016

Accepted 28 March 2017

Edited by J. F. van der Veen

Keywords: XAS beamline; X-ray absorption spectroscopy; Mg K-edge XANES; Al K-edge XANES; S K-edge XANES; Cu K-edge XANES; intermediate-energy X-ray beamline.

^aSynchrotron Light Research Institute, 111 University Avenue, Muang, Nakhon Ratchasima 30000, Thailand,^bFaculty of Science, Kasetsart University, 50 Ngam Wong Wan Road, Chatuchak, Bangkok 10900, Thailand,^cSchool of Physics, Suranaree University of Technology, Muang, Nakhon Ratchasima 30000, Thailand, and^dNational Nanotechnology Center, National Science and Technology Development Agency, 111 Thailand Science Park, Phahonyothin Road, Klong Luang, Pathum Thani 12120, Thailand.

*Correspondence e-mail: wantana@slri.or.th

The SUT-NANOTEC-SLRI beamline was constructed in 2012 as the flagship of the SUT-NANOTEC-SLRI Joint Research Facility for Synchrotron Utilization, co-established by Suranaree University of Technology (SUT), National Nanotechnology Center (NANOTEC) and Synchrotron Light Research Institute (SLRI). It is an intermediate-energy X-ray absorption spectroscopy (XAS) beamline at SLRI. The beamline delivers an unfocused monochromatic X-ray beam of tunable photon energy (1.25–10 keV). The maximum normal incident beam size is 13 mm (width) × 1 mm (height) with a photon flux of 3×10^8 to 2×10^{10} photons s^{-1} (100 mA) $^{-1}$ varying across photon energies. Details of the beamline and XAS instrumentation are described. To demonstrate the beamline performance, K-edge XANES spectra of MgO, Al₂O₃, S₈, FeS, FeSO₄, Cu, Cu₂O and CuO, and EXAFS spectra of Cu and CuO are presented.

1. Introduction

X-ray absorption spectroscopy (XAS) emerged as a new advanced characterization technique for material research in Thailand when the first XAS beamline, namely Beamline 8 (Klysubun *et al.*, 2012) of the Synchrotron Light Research Institute (SLRI) (Nakhon Ratchasima, Thailand), was successfully commissioned and opened publicly for academic and industrial users in 2006. After a few years of operation, the number of proposals requesting XAS beam time rapidly increased, resulting in inadequate beam time allocation. In 2009, Suranaree University of Technology (SUT), National Nanotechnology Center (NANOTEC) and SLRI jointly supported and launched a program to establish a central laboratory inside SLRI called SUT-NANOTEC-SLRI Joint Research Facility for Synchrotron Utilization, to provide a collaborative platform to utilize synchrotron techniques for researchers of the three parties and their collaborators. The program plan was to construct another XAS beamline at SLRI as the flagship under the name SUT-NANOTEC-SLRI beamline to be utilized in a time-sharing fashion among the three parties. The beamline was successfully constructed and commissioned in 2012. One-third of the beam time under SLRI quota is given to general users (both domestic and international) of SLRI *via* a regular beam time application, whereas one-third of the beam time is distributed by SUT for



Table 1

Specifications of selected XAS beamlines at other synchrotron facilities, working in soft and intermediate X-ray energy ranges.

Beamline	Facility	Energy range (keV)	Beam size (H × V)	Flux [photons s ⁻¹ (100 mA) ⁻¹]	Energy resolution	References
XAFCA	SSLS	1.2–12.8	1.5 mm × 0.5 mm	5.3 × 10 ⁹ †	5.1 × 10 ⁻⁴ ‡	Du <i>et al.</i> (2015)
DCMSX	SRRC	1.0–9.0	1.0 mm × 0.5 mm	1.5 × 10 ¹¹	1.3 × 10 ⁻⁴ §	Dann <i>et al.</i> (1998)
SXS	LNLS	0.8–4	2 mm × 3 mm	7 × 10 ⁸ to 2 × 10 ¹¹	7 × 10 ⁻⁴ to 9 × 10 ⁻⁴	Abbate <i>et al.</i> (1999)
SXRMB	CLS	1.7–10	260 μm × 230 μm	7 × 10 ⁹ to 1.3 × 10 ¹¹	1 × 10 ⁻⁴	Hu <i>et al.</i> (2010)
LUCIA	SOLEIL	0.8–8	2.5 μm × 2.5 μm	>10 ¹⁰	N/A	Flank <i>et al.</i> (2006)
ID21	ESRF	2–7.2	0.3 μm × 0.7 μm	10 ⁹ to 10 ¹⁰	1 × 10 ⁻⁴	Szlachetko <i>et al.</i> (2010)
DCM¶	CSRF¶	1.5–4.0	2.0 mm × 2.0 mm	1 × 10 ⁹ to 2 × 10 ¹⁰	N/A	Yang <i>et al.</i> (1992)
BL1A¶	UVSOR	0.8–4.0	2.0 mm × 1.0 mm	3 × 10 ⁸ to 4 × 10 ⁹	6.7 × 10 ⁻⁴	Hiraya <i>et al.</i> (1992), Shigemasa (2010)
BL7A¶	UVSOR	0.9–5.0	N/A	3 × 10 ⁶ to 2 × 10 ¹⁰	5.3 × 10 ⁻⁴	Murata <i>et al.</i> (1992), Kamada <i>et al.</i> (1996)

† Measured at 7 keV. ‡ Calculated at 10 keV. § Measured at 3.2 keV. ¶ Ceased operation.

their faculties, researchers and students and another one-third of the beam time is distributed by NANOTEC for their in-house researchers and collaborators. During the past four years, research output from the beamline has already resulted in 64 publications in international scientific journals. For the last two years, most of the research carried out at the beamline has involved investigations on valence states and local atomic structures in magnetic materials (*e.g.* Wongsaprom *et al.*, 2015; Sonsupap *et al.*, 2016; Kidkhunthod *et al.*, 2016; Luadthong *et al.*, 2016), dielectric materials (Boonlakhorn *et al.*, 2015; Jumpatam *et al.*, 2016; Meeporn *et al.*, 2016; Wongmaneerung *et al.*, 2016) and catalysts (Itthibenchapong *et al.*, 2015; Srifa *et al.*, 2015; Sanetuntikul *et al.*, 2015; Witoon *et al.*, 2016; Ketwong *et al.*, 2016).

The SUT-NANOTEC-SLRI beamline is classified as an intermediate-energy X-ray beamline working in the photon energy range 1.25–10 keV. It allows one to study the XAS of magnesium, aluminium, silicon, phosphorus, sulfur, chlorine, potassium, calcium and the first-row transition elements. There are only a small number of beamlines at other synchrotron facilities working in similar energy ranges. Table 1 gives examples of such beamlines with their technical specifications and references. Some of them have ceased operations. Similar to the DCM beamline at CSRF and the BL7A beamline at UVSOR, our beamline is equipped with a double-crystal monochromator (DCM) as the sole optical component for scanning photon energies while the other beamlines additionally employ X-ray mirrors for collimating and focusing their X-ray beams. The basic design of our DCM allowed in-house fabrication, use of different crystal types and a simple optical alignment. The installation of crystals and the fine-tuning process takes a shorter time (~1 h) than ordinary commercial DCMs. In the soft X-ray regime, the measurement becomes more challenging due to a much shorter penetration depth (compared with hard X-rays) through the instrumental windows and sample environment. Therefore, the XAS station was necessarily optimized for low-energy (soft) X-rays. The following sections provide the technical details of our beamline and its XAS station; beam characteristics (photon flux and energy resolution); the quality of XANES and EXAFS data demonstrated at the *K*-edges of magnesium, aluminium, sulfur and copper; and conclusions.

2. Beamline

The SUT-NANOTEC-SLRI beamline is connected to the vacuum chamber of bending magnet number 5 (BM5) of the SLRI 1.2 GeV synchrotron storage ring. The longitudinal source position of BM5 observed by the beamline is 7 cm after the BM5 edge, where the electron beam is deflected by 1.46° in the maximum 1.44 T magnetic field of BM5. In a user-service operation, the stored electron-beam current decays from 150 mA to 70 mA in 11 h. Fig. 1 shows a schematic view of the beamline. The first vacuum chamber is the heat absorber chamber (ABS) housing a water-cooled mask and a water-cooled copper block. The aperture size of the mask is 15 mm (width) × 7 mm (height) for passing a white beam of 6.5 mrad (h) × 3 mrad (v). Behind the ABS chamber, an attached side branch at the zero degree line is reserved for utilizing future insertion-device radiation. A water-cooled horizontal slit is installed behind the ABS for adjusting the white-beam width for downstream components. The white beam and Bremsstrahlung radiation can be shut off by a pneumatic drive lead block in the beam shutter chamber (BS). Four fluorescence screen monitor (FSM) chambers and an X-ray beam position monitor (XBPM) chamber are used for beam position measurements.

The DCM was in-house fabricated according to a Lemonnier design (Lemonnier *et al.*, 1978). The water-cooled first crystal and the uncooled second crystal are on a motorized rotation stage (Newport RV120HAHLT) driven by a motion controller (Newport MM4006). The center of rotation is on the surface of the first crystal. Several types of crystals are used in the DCM: KTiOPO₄(011), KTP ($2d = 10.955 \text{ \AA}$) covering 1.25 keV to 4.78 keV; InSb(111) ($2d = 7.481 \text{ \AA}$), 1.83 eV to 7.00 keV; and Ge(220) ($2d = 4.001 \text{ \AA}$), 3.44 keV to 10.00 keV. The Bragg angle (θ_B) can be scanned from 13.7° to 65.0° with a minimum increment ($\delta\theta_B$) of 0.001°. Using the differential form of Bragg's equation, $\delta E/E = \delta\theta_B \cot\theta_B$, a minimum energy step (δE) of our DCM can be determined for a given photon energy. For example, Mn *K*-edge (6539 eV) XAS spectra can be measured with actual energy steps of 0.2 eV, with good reproducibility. A mechanical cam, on which the second crystal travels, provides a vertical offset of 3.0 cm. Optical alignment of the two crystals is carried out with

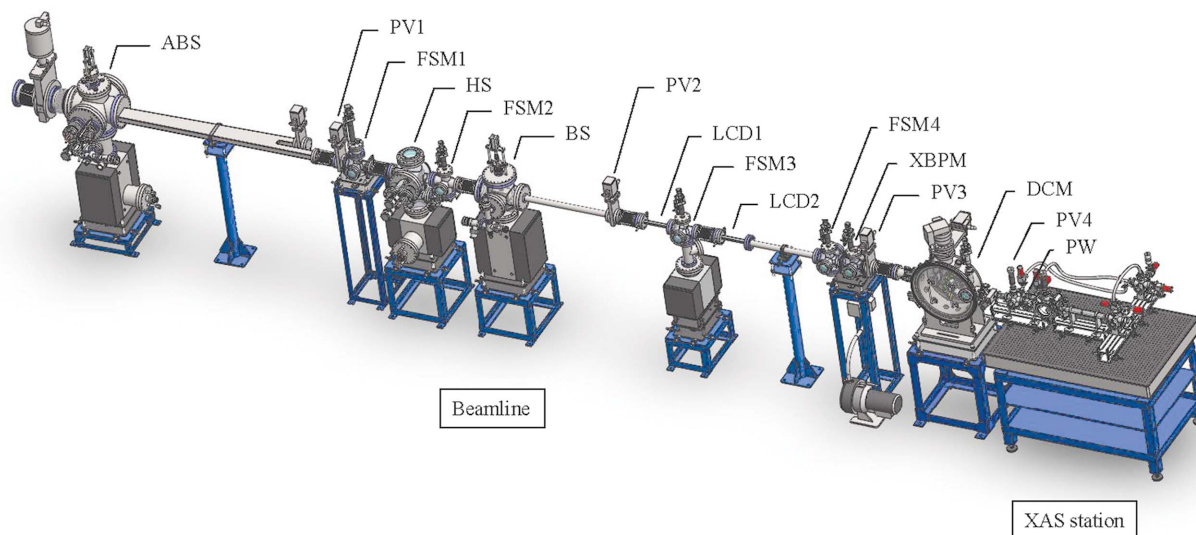


Figure 1

Schematic view of the SUT-NANOTEC-SLRI beamline, showing the heat absorber (ABS), pneumatic valves (PV1–PV4), fluorescent screen monitors (FSM1–FSM4), horizontal slit (HS), beam shutter (BS), low-conductance ducts (LCD1–LCD2), X-ray beam position monitor (XBPM), double-crystal monochromator (DCM) and polyimide window (PW).

motorized manipulators adjusting pitch angles of both crystals and roll angle of the second crystal. Energy resolution of the monochromatic X-ray beam is partly controlled by an entrance slit in the DCM, which is normally opened at 0.77 mm, corresponding to the angular beam divergence of $82 \mu\text{rad}$ in the vertical direction.

The vacuum of the beamline is maintained with three ion pumps (pumping speeds of 500 l s^{-1}) in the two front-end sections, an ion pump (300 l s^{-1}) attached to the FSM3 chamber, and two turbomolecular pumps (250 l s^{-1}) attached to the XBPM and DCM chambers. The differential pressure of four orders of magnitude between the front-end ultra-high vacuum (2.6×10^{-10} torr) and the DCM high vacuum (4.0×10^{-6} torr) is achieved using two small ducts of low conductance (LCD1 and LCD2). The lengths of LCD1 and LCD2 are 230 mm and inner dimensions are 17 mm (width) \times 8 mm (height) and 19.6 mm (width) \times 8.6 mm (height), respectively. LCD1 and LCD2, installed between the vacuum chambers (BS, FSM3 and XBPM), function as two differential pumping stages (Renier & Draperi, 1997; Klysubun *et al.*, 2007), and thus no beryllium (Be) window, which strongly absorbs low-energy X-rays, is needed. A polyimide window (PW) ($7.5 \mu\text{m}$ thick) is installed between the DCM chamber and the first ionization chamber of the XAS station. The inner diameter of the window is 13 mm, thus giving an angular beam divergence of 1.3 mrad in the horizontal direction. The beamline is operated with an interlock system using a programmable logic controller (Omron CS1G), which allows only safe opening and closing sequences of the pneumatic valves (PVs), the lead shutter in the BS chamber and the water-cooled copper absorber in the ABS chamber. The self-closing sequence would automatically turn on in case of vacuum failure detected by four cold cathode gauges and a full range gauge.

3. Experimental station

A photograph of the XAS station is shown in Fig. 2. XAS measurements can be conducted in either transmission or fluorescence-yield modes. The intensities of the incident X-ray beam (I_0) and the transmitted beam (I_t) are measured by the first (IC1) and second (IC2) gas-filled ionization chambers, respectively. The IC1 and IC2 chambers require 300 V DC to generate electrical currents when the X-ray beam passes through them. The full beam size at the sample chamber is 13 mm (width) \times 1 mm (height). Polypropylene windows (PPWs) ($6 \mu\text{m}$ thick) are used to seal the filled gas (nitrogen or argon) in the IC1 and IC2 chambers. Polypropylene is chosen because of its low X-ray absorption. The gas pressure is

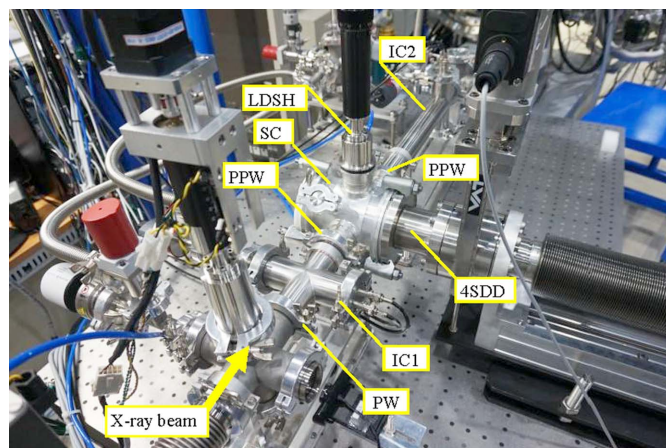


Figure 2

Photograph of the XAS station, showing the polyimide window (PW), ionization chambers (IC1 and IC2), polypropylene windows (PPW), sample chamber (SC), linear-drive sample holder (LDSH) and four-element silicon drift detector (4SDD).

specified according to Klysubun *et al.* (2012). In the transmission mode, the absorption (μx) of a probed element in a sample is determined by $\mu x = \ln(I_0/I_t)$, where μ is the linear absorption coefficient and x is the sample thickness (Bunker, 2010). For measurements below 5 keV, the sample chamber needs to have helium gas flowing in it to reduce air absorption. The sample thickness is recommended to be around one absorption length ($x = 1/\mu$). At this thickness, $\ln(I_0/I_t) = 1$ or $I_t/I_0 = 1/e$, and thus the sample absorbs 63% of the incident X-ray beam intensity (Calvin, 2013).

At 45° to the sample surface, and perpendicular to and in the same plane as the incoming X-ray beam, a four-element silicon drift (4SDD) detector (Vortex-ME4), with a 12.5 μm -thick Be window, is installed for fluorescence-mode XAS. The detector is integrated with a digital X-ray processor (XIA DXP-XMAP) and configured to selectively collect the fluorescence signal, I_{SCA} , of the K_α , L_α or M_α emission lines from a probed element in a sample. The dead-time of the 4SDD detector is corrected using the ratio of input count rate (ICR) to output count rate (OCR) recorded by the digital X-ray processor (Woicik *et al.*, 2010), $I_t = I_{\text{SCA}} \times \text{ICR}/\text{OCR}$. The absorption is given by $\mu = I_t/I_0$, which is only valid for diluted samples and thin concentrated samples (Calvin, 2013). For measurements of X-ray energy below 5 keV, the detector is attached to the sample chamber and operated under a steady flow of He gas.

The signal currents (I_0 and I_t) from each ionization chamber, typically having a value around 0.1 to 100 nA, are fed to current amplifiers (Keithley 428). With a proper gain used (10^7 V A^{-1} to 10^9 V A^{-1}), the output voltage is fed to a voltage-to-frequency converter (Nova N111VTF) to generate signal pulses at the rate of 0.1 MHz V^{-1} . A counter/timer device (NI PCI-6602) is used to record the number of signal pulses in a given dwell time synchronized with counting of I_t . A LabVIEW data acquisition program has been developed in-house to control all of the electronics and DCM scanning during the XAS data collection.

4. Performance for X-ray absorption spectroscopy

This section reports the photon flux and photon energy resolution of the monochromatic X-ray beam delivered by the beamline. Besides research samples, data of which can be found in the literature given in the *Introduction*, some test samples and standards were measured to demonstrate the quality of the XANES and EXAFS data.

4.1. Photon flux and photon energy resolution

We used the first ionization chamber IC1 (Fig. 2) to measure the experimental photon flux. It was filled with nitrogen gas or argon gas at a pressure so as to absorb 10% of the photon flux and generate an ionization current (Klysubun *et al.*, 2012). Based on the theory of photoionization (Knoll, 2010; Samson, 1999; Bunker, 2010), the relationship between the ionization current (I) and the photon flux (f) is expressed by

$$\frac{I}{e} = \frac{f[1 - \exp(-\sigma\rho L)]E}{w}, \quad (1)$$

where e is the electron charge, σ is the absorption cross section of the gas, ρ is the gas density, L is the absorption path length in the ionization chamber, E is the photon energy, and w is the average energy needed to create an electron-ion pair. The σ data were reported by Henke *et al.* (1993) and are available online through the Center for X-ray Optics (http://henke.lbl.gov/optical_constants). The w values for nitrogen and argon gases are 34.8 eV and 26.4 eV, respectively (Thompson & Vaughan, 2001). The gas density can be determined by the ideal gas law for a given gas pressure and gas temperature.

Fig. 3 shows the experimental photon flux of the full-sized monochromatic X-ray beam (13 mm \times 1 mm) as measured by the IC1 chamber. In general, our beamline experimentally gives a photon flux of 3×10^8 to 2×10^{10} photons s^{-1} (100 mA) $^{-1}$. At the magnesium K -edge (1303 eV) and aluminium K -edge (1560 eV), for which the KTP(011) crystals are employed, the beamline delivers an experimental photon flux of 9.1×10^8 and 1.5×10^9 photons s^{-1} (100 mA) $^{-1}$, respectively. The maximum photon flux of 2.2×10^{10} photons s^{-1} (100 mA) $^{-1}$, at the sulfur K -edge (2472 eV), is achieved with InSb(111) crystals. It should be noted that photon fluxes of the same order of magnitude are also available for studying phosphorus (2146 eV) and chlorine (2822 eV). Since InSb(111) crystals absorb X-rays at the L -edges of indium (3730, 3938 and 4238 eV) and antimony (4132, 4380 and 4698 eV), we alternatively use Ge(220) crystals for scanning photon energies from 3500 eV to 10000 eV. In this region, the experimental photon flux ranges from 3.3×10^8 to 8.2×10^9 photons s^{-1} (100 mA) $^{-1}$ and decreases with increasing photon energies. The photon fluxes of our beamline are comparable with those of the beamlines DCM, BL1A and BL7A (Table 1). It is noteworthy that the photon flux performance of a beamline is limited by the brightness of its X-ray source (bending magnet or insertion device). In general,

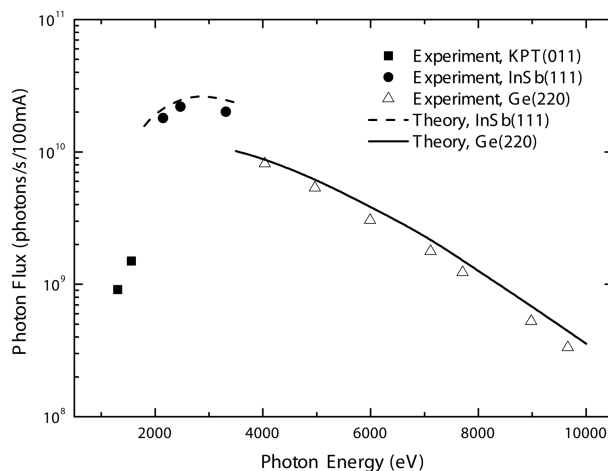


Figure 3 Experimental and theoretical photon fluxes of the full-sized monochromatic X-ray beam of the SUT-NANOTEC-SLRI beamline.

the brightness of a bending magnet or an insertion device is determined by its magnetic field strength, electron beam emittance and storage ring energy. In terms of brightness, our bending magnet BM5 is most comparable with the bending magnets of beamlines DCM and BL1A while the other beamlines take advantage of the brighter X-ray sources.

To determine the theoretical photon flux, a ray-tracing calculation was carried out using the *Shadow* software (Sanchez del Rio *et al.*, 2011). An X-ray source, consisting of 25000 rays, was simulated with spatial and angular distributions corresponding to the BM5 bending magnet and the SLRI storage ring specifications. Two optical components were defined as reflectors having perfect flat surfaces and diffraction properties of InSb(111) and Ge(220). It should be noted that *Shadow* does not implement a diffraction model for KTP crystals. The horizontal and vertical acceptances of the beamline ($1.3 \text{ mrad} \times 82 \text{ } \mu\text{rad}$) and optical transmission of the polyimide window (thickness of $7.5 \text{ } \mu\text{m}$) were also included in the calculation. The theoretical photon flux as a function of photon energy is shown in Fig. 3. It is higher than the actual measurement by a factor of 1.1 to 1.3. This indicates some loss of photon flux in the real optical configuration. An imperfect crystal surface resulting from a polishing procedure and a slope error introduced by crystal mounting probably decrease the photon flux of our beamline, as is the case for the SXRMB beamline at CLS (Table 1) during its preliminary commissioning (Hu *et al.*, 2010). Therefore, it will be beneficial to evaluate such possible influences for further improvement of our beamline in terms of the photon flux.

At a given Bragg angle (θ_B), a monochromatic X-ray beam diffracted by a beamline DCM has a certain photon energy distribution, $E \pm \Delta E/2$, and the percentage of the energy width ($\Delta E/E$) represents a respective energy resolution of the beamline. To experimentally determine ΔE , a rocking curve measurement is commonly performed by finely scanning (rocking) pitch angles of one of the DCM crystals and recording the diffracted intensity of the monochromatic beam as a function of the rocking angle (Abbate *et al.*, 1999; Kitamura *et al.*, 2003). An observed angular width of the rocking curve ($\Delta\theta$) is expressed as $\Delta\theta = (\Delta E/E)\tan(\theta_B)$ in the differential form of the Bragg equation. Due to the fact that our DCM is incapable of measuring a rocking curve as the pitch angles of the second crystal are not calibrated, an alternative measurement, proposed by Lytle *et al.* (1984), was used and can be described as follows. A XANES spectrum of argon gas was measured as shown in Fig. 4. The white-line peak, seen at 3206.5 eV, is attributed to the electronic transition from the $K(1s)$ level to the $N(4p)$ level (Watanabe, 1965), thus its theoretical width (ΔE_{th}) is the sum of the natural widths of the atomic K and N levels; $\Gamma_K + \Gamma_N$. For Ar gas, Γ_K is 0.68 eV whereas Γ_N is much smaller than Γ_K and thus negligible (Krause & Oliver, 1979). Therefore, ΔE_{th} of the Ar gas white line is approximately 0.68 eV. It can be seen that the observed width (ΔE_{obs}) is larger than ΔE_{th} . Fitting the white-line peak with a Lorentzian function (Watanabe, 1965), ΔE_{obs} is equal to 1.3 eV. The observed width is approximately a convoluted width of ΔE_{th} and the instrumental width (ΔE) of

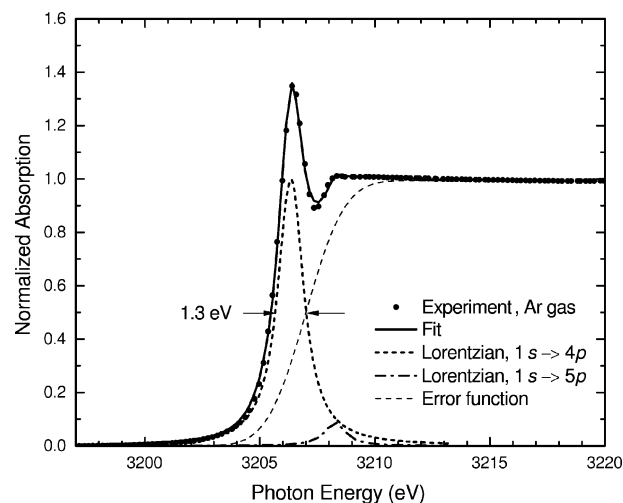


Figure 4
Ar K -edge XANES spectrum of Ar gas. The fit curve is the sum of the two Lorentzian functions and the error function.

our beamline; $\Delta E_{\text{obs}}^2 = \Delta E_{\text{th}}^2 + \Delta E^2$. Therefore, ΔE can be deduced and is equal to 1.1 eV (solid square in Fig. 6). As a result, the experimental energy resolution of our beamline at 3207 eV is approximately 3.4×10^{-4} . It is noteworthy that our energy resolution is clearly better than that of the LNLS SXS beamline (8×10^{-4}) at the same energy (Table 1).

Likewise, a XANES spectrum of KMnO_4 can be used to determine ΔE at the Mn K -edge. As shown in Fig. 5, the sharp pre-edge peak (6543 eV) is attributed to the $1s \rightarrow 3d$ electronic transition (Tolentino *et al.*, 2001). Its theoretical width is 2.66 eV, the sum of the natural width of the Mn K level (1.16 eV; Krause & Oliver, 1979) and the natural width of the $3d$ valence band (1.5 eV; Tolentino *et al.*, 2001). The observed width (FWHM) is 3.39 eV as shown in Fig. 5. The instrumental width of the beamline can be deconvoluted from the observed width and is equal to 2.10 eV (open square in Fig. 6). This corresponds to an energy resolution of 3.2×10^{-4} at 6543 eV.

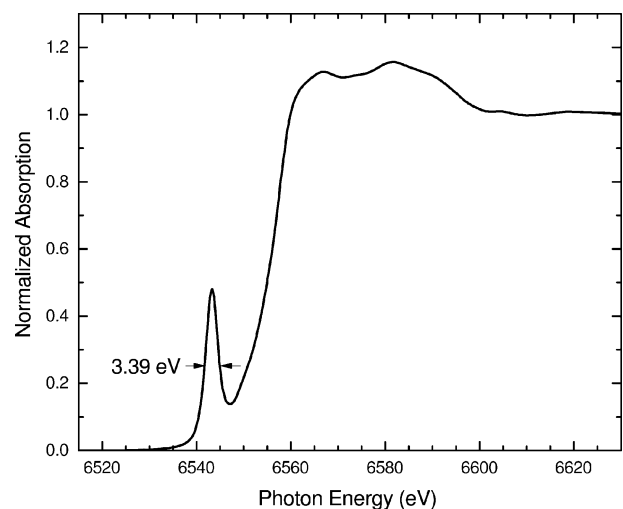
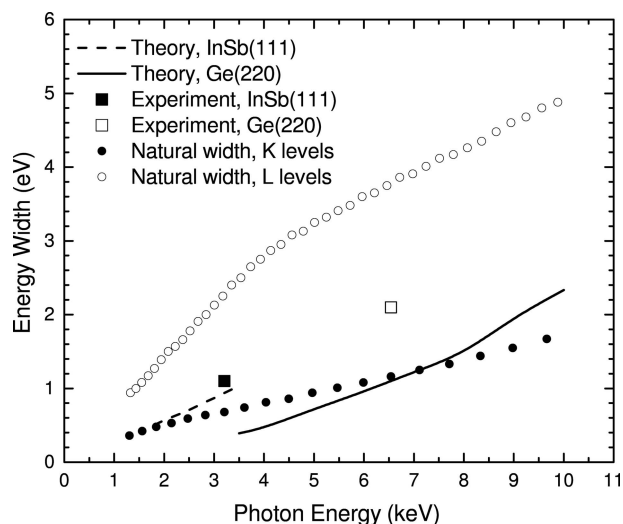


Figure 5
Mn K -edge XANES spectrum of KMnO_4 .


Figure 6

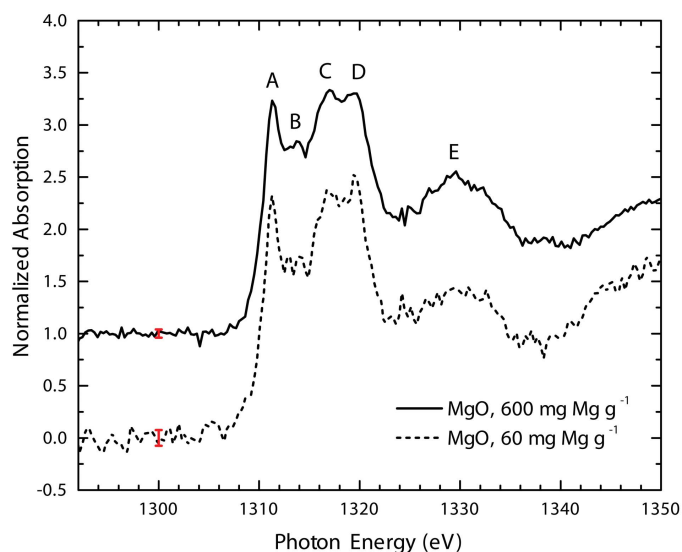
Experimental and theoretical energy widths of the monochromatic X-ray beam of the SUT-NANOTEC-SLRI beamline and natural widths of the atomic K and L levels.

We expect the broadening effects on the K -edge XANES spectra to arise significantly from the instrumental energy widths of the beamline as they are larger than the natural widths of the atomic K levels (solid circles in Fig. 6). On the contrary, the natural widths of the atomic L_3 levels (open circles in Fig. 6) are primarily responsible for the broadening of the L_3 -edge XANES spectra. The ray-tracing calculations also predict an instrumental width of the beamline as a function of photon energy, in the case of the perfect optical configuration as discussed previously. The ideal instrumental widths are shown in Fig. 6 by a dashed line and a solid line for InSb(111) and Ge(220), respectively. They are considerably smaller than the actual instrumental widths. A further investigation is needed to identify causes of error affecting the energy resolutions of the beamline and whether they relate to the reduction of the photon flux.

4.2. Magnesium and aluminium K -edge XANES

XANES measurements in the energy range of the K -edges of magnesium (1303 eV) and aluminium (1560 eV) are challenging because the low-energy photons are easily absorbed by a sample and its mounting materials. Preparing a transmission sample becomes difficult, if not impossible, since the thickness of one absorption length is about 1 μm or even smaller. For example, such thicknesses are 1.1 μm and 0.7 μm for Mg metal and MgO, respectively. When a powder sample is used, a supporting tape such as polyimide tape, on which the sample is spread, further reduces the photon intensity. The polypropylene window of the IC1 chamber also absorbs the photon flux by about 40% at 1303 eV. Therefore, such a XANES experiment at our beamline can only be carried out in the fluorescence-yield mode.

Fig. 7 shows Mg K -edge XANES spectra of pure MgO (Mg concentration of 600 mg Mg g^{-1}) and diluted MgO


Figure 7

Normalized Mg K -edge XANES spectra of pure MgO (600 mg Mg g^{-1}) and diluted MgO (60 mg Mg g^{-1}). Peaks A–E are described in the text. Error bars represent magnitudes of noise estimated for each spectrum. The upper spectrum is vertically shifted by 1.0.

(60 mg Mg g^{-1}). Each spectrum was averaged from five scans. Each scan was collected with energy steps of 0.3 eV and a dwell time of 30 s for each energy. A photon energy calibration was performed using the white-line energy of MgO at 1311.3 eV (Li *et al.*, 1999). The diluted MgO was prepared by mixing 10 mg of MgO with 90 mg of boron nitride (BN) using a mortar and pestle. The pure and diluted MgO samples were pressed into pellets for the XANES measurements. Denoted by A, B, C, D and E in Fig. 7, all characteristic peaks of MgO are clearly recognized in our XANES spectrum and correspond to those recorded by Aritani *et al.* (2001) and Takata *et al.* (2001) using the BL7A and BL1A beamlines at UVSOR, respectively (Table 1). It should be noted that their XANES measurements were carried out in a vacuum using electron-yield modes. The energies of the peaks A, B, C, D and E, in our MgO spectrum, are 1311.3 eV, 1313.8 eV, 1317.1 eV, 1319.3 eV and 1329.4 eV, respectively, whereas those of the BL7A spectrum are shifted by $-13.7 \text{ eV} \pm 0.4 \text{ eV}$ due to a different photon energy calibration used. In terms of signal-to-noise ratio, our MgO data are as noisy as the BL1A data and noisier than the BL7A data. However, we can correctly identify the main features of MgO.

Experimental noise appears as random fluctuations in the normalized spectrum of pure MgO (Fig. 7). The magnitudes can be estimated by the standard deviation (σ) of normalized μ in a pre-edge region of 1292 eV to 1305 eV. Consequently, σ was found to be 0.039 shown as an error bar in Fig. 7. The signal-to-noise ratios of the peaks A, B, C, D and E, as estimated by their μ/σ values, are 57, 47, 60, 59 and 39, respectively. Using the same evaluation for the normalized spectrum of the diluted MgO, σ is 0.076, and the signal-to-noise ratios of the peaks A, B, C, D and E are 31, 22, 31, 33 and 19, respectively. It is noteworthy that the signal-to-noise ratios are not linearly decreased with the decrease of Mg concentration.

Fig. 8 shows Al *K*-edge XANES spectra of diluted Al₂O₃ with Al concentrations of 5.3 mg Al g⁻¹ and 53 mg Al g⁻¹. Each spectrum was averaged from five scans. Each scan was collected with energy steps of 0.3 eV and a dwell time of 30 s for each energy. A photon energy calibration was performed using the *K*-edge energy of Al metal at 1560 eV (Li *et al.*, 1995). The diluted Al₂O₃ samples were prepared, similar to the case of MgO. We mixed 1 mg of Al₂O₃ with 99 mg of BN to yield 5.3 mg Al g⁻¹, and 10 mg of Al₂O₃ with 90 mg of BN to yield 53 mg Al g⁻¹. Each diluted Al₂O₃ sample was pressed into a pellet for the XANES measurements. Signal-to-noise ratios of the two spectra of 5.3 mg Al g⁻¹ and 53 mg Al g⁻¹ are approximately 57–73 and 170–227, respectively. Our diluted Al₂O₃ spectra are qualitatively similar to the Al *K*-edge spectra of pure Al₂O₃ (530 mg Al g⁻¹) previously published by Li *et al.* (1995), Takata *et al.* (2001) and Manuel *et al.* (2012). Their spectra were measured in electron-yield modes using the beamlines DCM, BL1A and LUCIA, respectively (Table 1). According to an interpretation by Li *et al.* (1995), two strong peaks seen in our spectra at 1568.7 eV and 1572.4 eV (denoted by *A* and *B* in Fig. 8) are attributed to the 1*s* → *t*_{1*u*} and 1*s* → *t*_{2*g*} electronic transitions, respectively, whereas a weak peak at 1576.8 eV (denoted by *C*) arises from a multiple-scattering effect. The energies of the peaks *A*, *B* and *C* reported by Li *et al.* (1995) are lower than ours by 0.3 eV, 0.8 eV and 0.9 eV, respectively. It is noteworthy that, at the lower Al concentration (53 mg Al g⁻¹), we were able to record the Al₂O₃ spectrum slightly noisier than the Al₂O₃ spectra of higher Al concentration (530 mg Al g⁻¹) from those beamlines. In addition, the signal-to-noise ratios of the Al₂O₃ (5.3 mg Al g⁻¹) spectrum are close to those of the MgO (60 mg Mg g⁻¹) spectrum, and therefore our beamline is more efficient for XANES measurements at the Al *K*-edge than it is for the Mg *K*-edge. This is basically due to the higher photon flux available at the Al *K*-edge (Fig. 3).

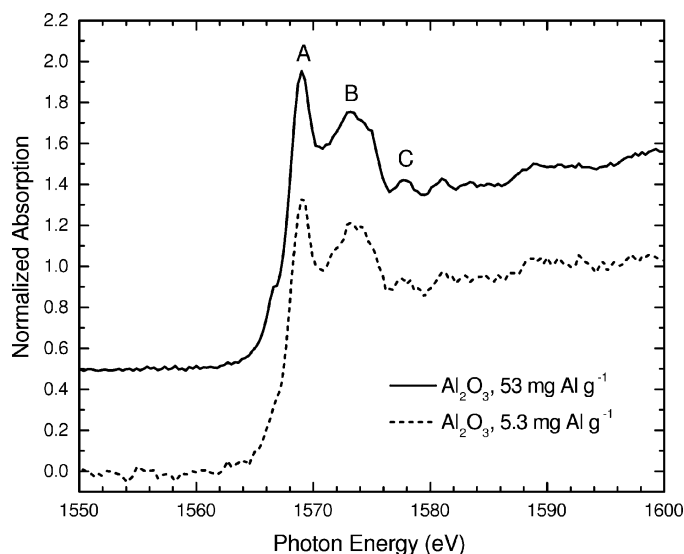


Figure 8
Normalized Al *K*-edge XANES spectra of diluted Al₂O₃ (53 mg Al g⁻¹ and 5.3 mg Al g⁻¹). Peaks *A*–*C* are described in the text. The upper spectrum is vertically shifted by 0.5.

4.3. Sulfur *K*-edge XANES

Sulfur is one of the most abundant elements existing in a large variety of organic and inorganic species with formal oxidation states of sulfur ranging from –2 to +6 (Prietzl *et al.*, 2011). The SUT-NANOTEC-SLRI beamline has the highest photon flux at the sulfur *K*-edge, and is thereby powerful for sulfur speciation. For pure standards and concentrated samples, S *K*-edge XANES spectra can be measured in the transmission mode, for which the ideal thickness of one absorption length ($x = 1/\mu$) can be practically prepared using powder samples. Fig. 9 shows S *K*-edge XANES spectra of S₈ and FeSO₄·7H₂O measured in transmission mode. Characteristic peaks of S₈ and FeSO₄·7H₂O are clearly visible and their spectral shapes resemble those reported by Dann *et al.* (1998), Figueiredo & Silva (2009) and Prietzl *et al.* (2011). Their S *K*-edge XANES spectra were measured at the DCMSX beamline at SRRC, the ID21 beamline at ESRF and the BL8 beamline at SLRI (Klysubun *et al.*, 2012), respectively.

To demonstrate the performance of our beamline for sulfur speciation, we used a test sample (T1) consisting of three oxidation states of sulfur (–2, 0 and +6). The sample T1 was prepared by mixing 6 mg of FeS, 2 mg of S₈ and 2 mg of FeSO₄·7H₂O. Therefore, the nominal atomic percentages of S²⁻, S⁰ and S⁶⁺ in sample T1 are 0.50, 0.45 and 0.05, respectively. A four-digit balance was used for weighing, and a mortar and pestle were used for grinding the mixture. The sample T1 was diluted using 1 mg of T1 and 99 mg of BN and mixed with a mortar and pestle. Finally, the diluted mixture was pressed into a pellet for the XANES experiment in the fluorescence yield mode. The three standards (FeS, S₈ and FeSO₄·7H₂O) were diluted, prepared in the same way and measured under the same experimental conditions, as is the case for the diluted sample T1. We used a linear combination fitting (LCF) tool in the *Athena* software (Ravel & Newville, 2005) to determine the percentages of sulfur atoms in each oxidation state present in sample T1. The S *K*-edge XANES

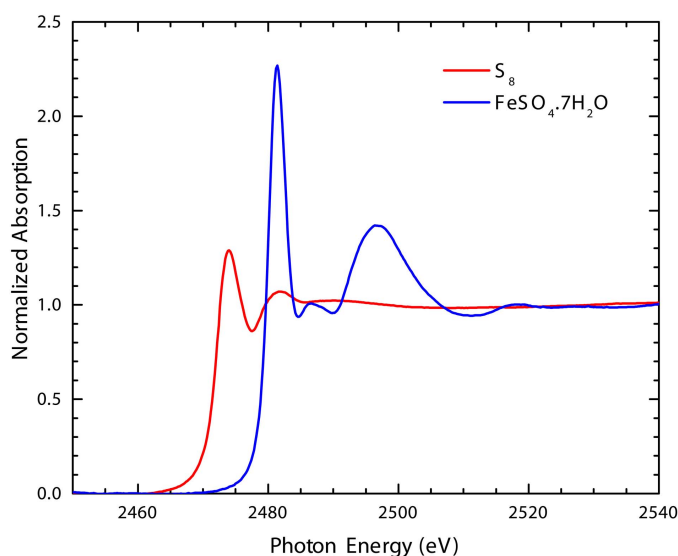


Figure 9
Normalized S *K*-edge XANES spectra of S₈ and FeSO₄·7H₂O.

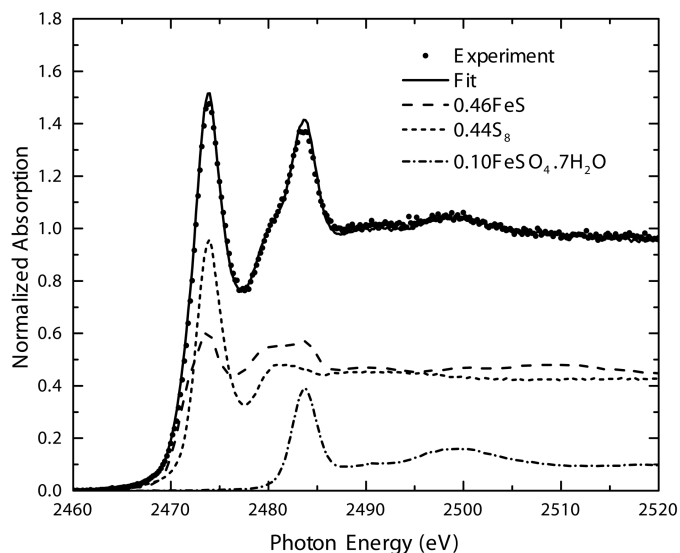


Figure 10
The best-fit curve and its LCF components of the T1 sample.

spectra of the three standards were used as fitting components. Fig. 10 shows the best-fit curve of T1 as the sum of its LCF components scaled by the atomic percentages of sulfur (0.46FeS, 0.44S₈ and 0.10FeSO₄·7H₂O). The best-fit curve reproduces very well the experimental T1 spectrum with a very small fractional misfit factor of 0.00035. The LCF speciation results are very close to nominal sulfur percentages. The slight discrepancy is probably due to inaccuracy of the four-digit balance and non-uniformity of the T1 sample. Particle size and concentration effects from the sample-preparation procedure can also introduce distortion of the XANES data (Morgan *et al.*, 2009). However the accuracy of our S speciation is markedly better than that reported by Prietzel *et al.* (2011) for a large set of different mixtures.

4.4. Copper K-edge XANES and EXAFS

Fig. 11 shows Cu K-edge XANES spectra of Cu metal (5 μm-thick foil), Cu₂O and CuO. The data were collected in the transmission mode. The fine structures are clearly observed in all samples and consistent with those previously reported (Du *et al.*, 2015; Yalovega *et al.*, 2016; Klysubun *et al.*, 2015; Gaur *et al.*, 2009). The insert of Fig. 11 shows the shoulder peaks (8981.3 eV) of Cu metal recorded by Du *et al.* (2015) at the XAFCA beamline (Table 1) and Ravel & Newville (2005) at the X23A2 beamline at the National Synchrotron Light Source (Golovchenko *et al.*, 1981), in comparison with our data. Our peak is as broad as the XAFCA peak and considerably broader than the X23A2 peak. Therefore, the energy resolutions of our beamline given by Ge(220) crystals and the XAFCA beamline by Si(111) are approximately equal at the Cu K-edge. It should be noted that the better energy resolution of X23A is achieved by Si(311). However, the lower energy resolution of our beamline is clearly sufficient for detecting the sharper shoulder peak (8982.7 eV) of the 1s → 4p electronic transition in Cu₂O. To

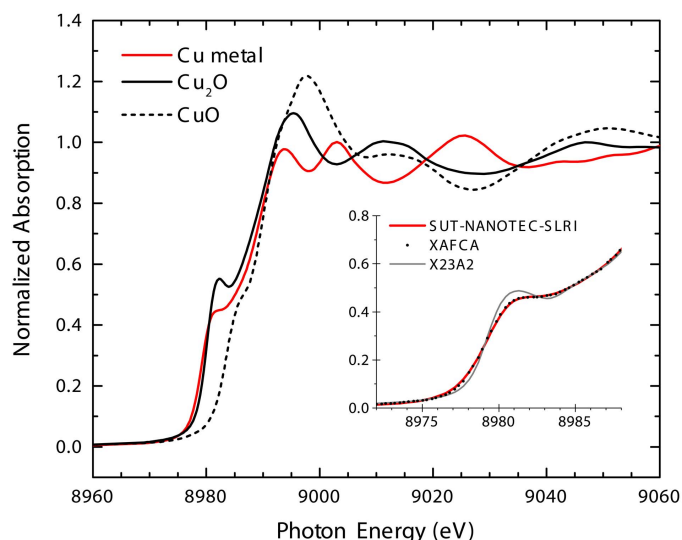


Figure 11
Normalized Cu K-edge XANES spectra of Cu metal, Cu₂O and CuO measured from the SUT-NANOTEC-SLRI beamline. The insert shows the shoulder peaks of Cu metal recorded from beamlines SUT-NANOTEC-SLRI, XAFCA and X23A2.

demonstrate the EXAFS performance of our beamline, K-edge EXAFS spectra of Cu metal and CuO were measured in the transmission mode. Fig. 12 shows the Fourier-transformed EXAFS spectra of the Cu metal and CuO in comparison with the data from beamlines XAFCA and X23A2. The Fourier transformation (FT) was carried out using the *Athena* software (Ravel & Newville, 2005) with the same FT parameters: Hanning window, *k*-range of 3 to 12 Å⁻¹, *k*² weight, *dk* = 2 Å⁻¹ and *R*_{bkg} = 1. It can be seen that the EXAFS data from the three beamlines are consistent in terms of observed peak position and EXAFS magnitude in the *R*-space. For quantitative assessment, the fractional mismatch between our EXAFS data, |χ(*R*)|, and those from the other two beamlines,

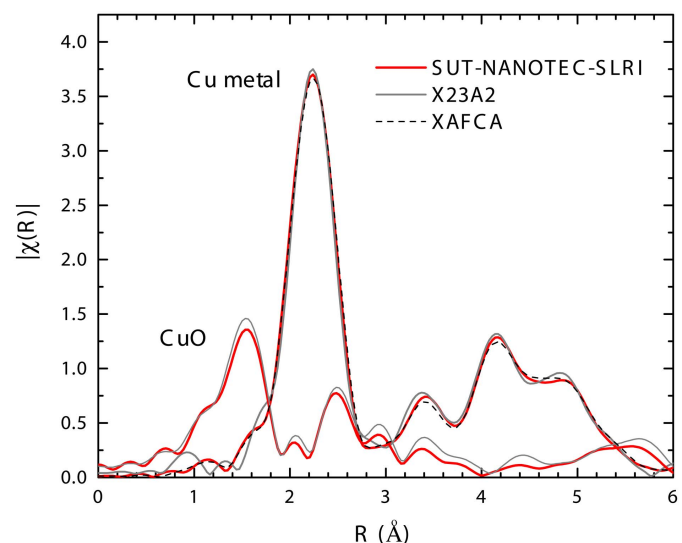


Figure 12
Magnitude of Fourier-transformed χ(*R*) spectra of Cu metal and CuO measured from beamlines SUT-NANOTEC-SLRI, XAFCA and X23A2.

$|\chi(R)|'$, was calculated as $\sum[|\chi(R)| - |\chi(R)'|^2]/\sum|\chi(R)|^2$, where the summation was computed over all data points between $R = 0$ and $R = 6 \text{ \AA}$. In the case of the Cu metal EXAFS, the resultant fractional mismatch was 0.00075 and 0.0042, for the XAFCA and X23A2 data, respectively. In the case of the CuO EXAFS, the fractional mismatch was 0.0192 for the X23A data. Even though the photon flux of our beamline at the Cu K -edge is considerably lower than those of the XAFCA and X23A2 beamlines, we have demonstrated that our EXAFS data are quantitatively comparable with the EXAFS data from the two high-performance beamlines.

5. Conclusions

The design and specifications of the SUT-NANOTEC-SLRI beamline and its XAS station have been reported. The working photon energy range is 1.25 to 10 keV. The available photon fluxes [3×10^8 to 2×10^{10} photons s^{-1} ($100 \text{ mA})^{-1}$] and photon energy resolutions given by the KTP(011), InSb(111) and Ge(220) DCM are practical for conventional XAS measurements as shown in Figs. 7–12. For the Mg and Al K -edges, the XANES data can be collected in fluorescence-yield mode with recommended concentrations higher than 60 mg Mg g^{-1} and 5.3 mg Al g^{-1} . For XAS measurements at the K -edges of Si, P, S, Cl, Ca and the first-row transition elements, both transmission and fluorescence-yield modes can be applied depending on sample characteristics. We have demonstrated that the SUT-NANOTEC-SLRI beamline and its XAS station can provide XANES and EXAFS data in good agreement with those from the other beamlines of comparable energy ranges (Table 1) and the hard X-ray beamline X23A2. Therefore, this paper can be used as a reference point and introduces a choice of intermediate-energy X-ray beamlines for the international XAS users' community.

Acknowledgements

The authors acknowledge Denchay Bumrungrkoh and Samrerng Duangnil for supervision of the in-house fabrication of the beamline and XAS components. Beamline control software has been developed by Nattawat Yachum and Narupon Wongprachanukul. Sompin Mahakot, Somboonsup Rodporn, and Dechmongkhon Keawsuwan are thanked for the XAS measurements. Yonghua Du and Ping Yang are acknowledged for providing the EXAFS data of Cu metal from the XAFCA beamline. Bruce Ravel is acknowledged for providing the EXAFS data of Cu metal and CuO from the X23A2 beamline at NSLS, a US Department of Energy (DOE) Office of Science User Facility operated for the DOE Office of Science by Brookhaven National Laboratory under Contract No. DE-AC02-98CH10886. Garnet Hoyes and Professor Jörg Prietzel are acknowledged for grammar correction. This research was funded by SUT-NANOTEC-SLRI Joint Research Facility for Synchrotron Utilization.

References

- Abbate, M., Vicentin, F. C., Compagnon-Cailhol, V., Rocha, M. C. & Tolentino, H. (1999). *J. Synchrotron Rad.* **6**, 964–972.
- Aritani, H., Yamada, H., Yamamoto, T., Tanaka, T. & Imamura, S. (2001). *J. Synchrotron Rad.* **8**, 593–595.
- Boonlakhorn, J., Kidkhunthod, P., Putasaeng, B., Yamwong, T., Thongbai, P. & Maensiri, S. (2015). *Appl. Phys. A*, **120**, 89–95.
- Bunker, G. (2010). *Introduction to XAFS*. New York: Cambridge University Press.
- Calvin, S. (2013). *XAFS for Everyone*. New York: CRC Press.
- Dann, T.-E., Chung, S.-C., Huang, L.-J., Juang, J.-M., Chen, C.-I. & Tsang, K.-L. (1998). *J. Synchrotron Rad.* **5**, 664–666.
- Du, Y., Zhu, Y., Xi, S., Yang, P., Moser, H. O., Breese, M. B. H. & Borgna, A. (2015). *J. Synchrotron Rad.* **22**, 839–843.
- Figueiredo, M. O. & da Silva, T. P. (2009). *Eur. J. Mineral.* **21**, 79–83.
- Flank, A.-M., Cauchon, G., Lagarde, P., Bac, S., Janousch, M., Wetter, R., Dubuisson, J.-M., Idir, M., Langlois, F., Moreno, T. & Vantelon, D. (2006). *Nucl. Instrum. Methods Phys. Res. B*, **246**, 269–274.
- Gaur, A., Shrivastava, B. D. & Joshi, S. K. (2009). *J. Phys.* **190**, 012084.
- Golovchenko, J. A., Levesque, R. A. & Cowan, P. L. (1981). *Rev. Sci. Instrum.* **52**, 509–516.
- Henke, B. L., Gullikson, E. M. & Davis, J. C. (1993). *At. Data Nucl. Data Tables*, **54**, 181–342.
- Hiraya, A., Horigome, T., Okada, N., Mizutani, N., Sakai, K., Matsudo, O., Hasumoto, M., Fukui, K. & Watanabe, M. (1992). *Rev. Sci. Instrum.* **63**, 1264–1268.
- Hu, Y. F., Coulthard, I., Chevrier, D., Wright, G., Igarashi, R., Sitnikov, A., Yates, B. W., Hallin, E. L., Sham, T. K. & Reiningger, R. (2010). *AIP Conf. Proc.* **1234**, 343–346.
- Itthibenchapong, V., Ratanatawanate, C., Oura, M. & Faungnawakij, K. (2015). *Catal. Commun.* **68**, 31–35.
- Jumpatam, J., Mooltang, A., Putasaeng, B., Kidkhunthod, P., Chanlek, N., Thongbai, P. & Maensiri, S. (2016). *Ceram. Int.* **42**, 16287–16295.
- Kamada, M., Hosaka, M., Gejo, T. & Hagiwara, H. (1996). *UVSOR Activity Report 1996*. UVSOR Facility, Okazaki, Japan.
- Ketwong, P., Kidkhunthod, P. & Pookmanee, P. (2016). *Integr. Ferroelectr.* **175**, 9–17.
- Kidkhunthod, P., Nilmoung, S., Mahakot, S., Rodporn, S., Phumying, S. & Maensiri, S. (2016). *J. Magn. Magn. Mater.* **401**, 436–442.
- Kitamura, M., Yoshikawa, H., Mochizuki, T., Vlaicu, A. M., Nisawa, A., Yagi, N., Okui, M., Kimura, M., Tanaka, T. & Fukushima, S. (2003). *Adv. X-ray Anl.* **46**, 326–331.
- Klysubun, W., Hauzenberger, A., Ravel, B., Klysubun, P., Huang, Y., Wongtepa, W. & Sombunchoo, P. (2015). *X-ray Spectrom.* **44**, 116–123.
- Klysubun, W., Sombunchoo, P., Deenan, W. & Kongmark, C. (2012). *J. Synchrotron Rad.* **19**, 930–936.
- Klysubun, W., Sombunchoo, P., Wongprachanukul, N., Tarawarakarn, P., Klinkhieo, S., Chaiprapa, J. & Songsiririthigul, P. (2007). *Nucl. Instrum. Methods Phys. Res. A*, **582**, 87–89.
- Knoll, G. F. (2010). *Radiation Detection and Measurement*. New York: John Wiley and Sons.
- Krause, M. O. & Oliver, J. H. (1979). *J. Phys. Chem. Ref. Data*, **8**, 329–338.
- Lemonnier, M., Collet, O., Depautex, C., Esteva, J. & Raoux, D. (1978). *Nucl. Instrum. Methods*, **152**, 109–111.
- Li, D., Bancroft, G. M., Fleet, M. E., Feng, X. H. & Pan, Y. (1995). *Am. Mineral.* **80**, 432–440.
- Li, D., Peng, M. & Murata, T. (1999). *Can. Mineral.* **37**, 199–206.
- Luadthong, C., Khemthong, P., Nualpaeng, W. & Faungnawakij, K. (2016). *Appl. Catal. Gen.* **525**, 68–75.
- Lytle, F. W., Greggor, R. B., Sandstrom, D. R., Marques, E. C., Wong, J., Spiro, C. L., Huffman, G. P. & Huggins, F. E. (1984). *Nucl. Instrum. Methods Phys. Res. A*, **226**, 542–548.

- Manuel, D., Cabaret, D., Brouder, C., Saintavit, P., Bordag, A. & Trcera, N. (2012). *HAL-00681349*. HAL open access archive: <http://hal.archives-ouvertes.fr/hal-00681349>.
- Meeporn, K., Maensiri, S. & Thongbai, P. (2016). *Appl. Surf. Sci.* **380**, 67–72.
- Morgan, K. E., Burton, E. D., Cook, P., Raven, M. D., Fitzpatrick, R. W., Bush, R., Sullivan, L. A. & Hocking, R. K. (2009). *J. Phys. Conf. Ser.* **190**, 012144.
- Murata, T., Matsukawa, T., Naoé, S., Horigome, T., Matsudo, O. & Watanabe, M. (1992). *Rev. Sci. Instrum.* **63**, 1309–1312.
- Prietzl, J., Botzaki, A., Tyufekchieva, N., Brettholle, M., Thieme, J. & Klysubun, W. (2011). *Environ. Sci. Technol.* **45**, 2878–2886.
- Ravel, B. & Newville, M. (2005). *J. Synchrotron Rad.* **12**, 537–541.
- Renier, M. & Draperi, A. (1997). *Vacuum*, **48**, 405–407.
- Samson, J. A. R. (1999). *Vacuum Ultraviolet Spectroscopy*. London: Academic Press.
- Sanchez del Rio, M., Canestrari, N., Jiang, F. & Cerrina, F. (2011). *J. Synchrotron Rad.* **18**, 708–716.
- Sanetuntikul, J., Chuaicham, C., Choi, Y.-W. & Shanmugam, S. (2015). *J. Mater. Chem. A*, **3**, 15473–15481.
- Shigemasa, E. (2010). *UVSOR Activity Report 2010*. UVSOR Facility, Okazaki, Japan.
- Sonsupap, S., Kidkhunthod, P., Chanlek, N., Pinitsoontorn, S. & Maensiri, S. (2016). *Appl. Surf. Sci.* **380**, 16–22.
- Srifa, A., Viriya-empikul, N., Assabumrungrat, S. & Faungnawakij, K. (2015). *Catal. Sci. Technol.* **5**, 3693–3705.
- Szlachetko, J., Cotte, M., Morse, J., Salomé, M., Jagodzinski, P., Dousse, J.-C., Hoszowska, J., Kayser, Y. & Susini, J. (2010). *J. Synchrotron Rad.* **17**, 400–408.
- Takata, Y., Shigemasa, E. & Kosugi, N. (2001). *J. Synchrotron Rad.* **8**, 351–353.
- Thompson, A. C. & Vaughan, D. (2001). *X-ray Data Booklet*. California: Lawrence Berkeley National Laboratory.
- Tolentino, H. C. N., Ramos, A. Y., Alves, M. C. M., Barrea, R. A., Tamura, E., Cezar, J. C. & Watanabe, N. (2001). *J. Synchrotron Rad.* **8**, 1040–1046.
- Watanabe, T. (1965). *Phys. Rev.* **139**, A1747–A1751.
- Witoon, T., Kachaban, N., Donphai, W., Kidkhunthod, P., Faungnawakij, K., Chareonpanich, M. & Limtrakul, J. (2016). *Energy Convers. Manage.* **118**, 21–31.
- Woicik, J. C., Ravel, B., Fischer, D. A. & Newburgh, W. J. (2010). *J. Synchrotron Rad.* **17**, 409–413.
- Wongmaneeerung, R., Tipakontitukul, R., Jantaratana, P., Bootchanont, A., Jutimoosik, J., Yimnirun, R. & Ananta, S. (2016). *Mater. Res. Bull.* **75**, 91–99.
- Wongsaprom, K., Sonsupap, S., Maensiri, S. & Kidkhunthod, P. (2015). *Appl. Phys. A*, **121**, 239–244.
- Yalovega, G., Funik, A., Myasoedova, T. & Brzhezinskaya, M. (2016). *J. Phys. Conf. Ser.* **71**, 012055.
- Yang, B. X., Middleton, F. H., Olsson, B. G., Bancroft, G. M., Chen, J. M., Sham, T. K., Tan, K. H. & Wallace, J. D. (1992). *Nucl. Instrum. Methods Phys. Res. A*, **316**, 422–436.